

KeyPosS: Plug-and-Play Facial Landmark Detection through GPS-Inspired True-Range Multilateration

Xu Bao*
baoxu@email.szu.edu.cn
DAMO Academy, Alibaba Group

Zhi-Qi Cheng*[†]
zhiqi@cs.cmu.edu
Carnegie Mellon University

Jun-Yan He*[†]
leyuan.hjy@alibaba-inc.com
DAMO Academy, Alibaba Group

Wangmeng Xiang
wangmeng.xwm@alibaba-inc.com
DAMO Academy, Alibaba Group

Chenyang Li
lichenyang.scut@foxmail.com
DAMO Academy, Alibaba Group

Jingdong Sun
jingdons@andrew.cmu.edu
Carnegie Mellon University

Hanbing Liu
liuhb21@mails.tsinghua.edu.cn
Tsinghua University

Wei Liu
ustclwxx@gmail.com
DAMO Academy, Alibaba Group

Bin Luo
luwu.lb@alibaba-inc.com
DAMO Academy, Alibaba Group

Yifeng Geng
cangyu.gyf@alibaba-inc.com
DAMO Academy, Alibaba Group

Xuansong Xie
xingtong.xxs@taobao.com
DAMO Academy, Alibaba Group

ABSTRACT

Accurate facial landmark detection is critical for facial analysis tasks, yet prevailing heatmap and coordinate regression methods grapple with prohibitive computational costs and quantization errors. Through comprehensive theoretical analysis and experimentation, we identify and elucidate the limitations of existing techniques. To overcome these challenges, we pioneer the application of True-Range Multilateration, originally devised for GPS localization, to facial landmark detection. We propose KeyPoint Positioning System (KeyPosS) - the first framework to deduce exact landmark coordinates by triangulating distances between points of interest and anchor points predicted by a fully convolutional network. A key advantage of KeyPosS is its plug-and-play nature, enabling flexible integration into diverse decoding pipelines. Extensive experiments on four datasets demonstrate state-of-the-art performance, with KeyPosS outperforming existing methods in low-resolution settings despite minimal computational overhead. By spearheading the integration of Multilateration with facial analysis, KeyPosS marks a paradigm shift in facial landmark detection. The code is available at <https://github.com/zhiqi/KeyPosS>.

CCS CONCEPTS

• **Computing methodologies** → **Facial landmark detection**.

*Denotes equal contributions

[†]Zhi-Qi Cheng and Jun-Yan He are the corresponding authors

Permission to make digital or hard copies of all or part of this work for personal or classroom use is granted without fee provided that copies are not made or distributed for profit or commercial advantage and that copies bear this notice and the full citation on the first page. Copyrights for components of this work owned by others than the author(s) must be honored. Abstracting with credit is permitted. To copy otherwise, or republish, to post on servers or to redistribute to lists, requires prior specific permission and/or a fee. Request permissions from permissions@acm.org.

MM '23, October 29–November 3, 2023, Ottawa, ON, Canada

© 2023 Copyright held by the owner/author(s). Publication rights licensed to ACM.

ACM ISBN 979-8-4007-0108-5/23/10...\$15.00

<https://doi.org/10.1145/3581783.3612366>

KEYWORDS

Facial Landmark Detection, True-Range Multilateration

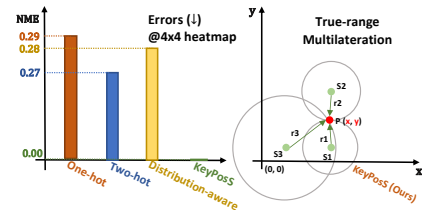


Figure 1: Comparison of the facial landmark detection strategies. On the left, we highlight the accuracy of our method, KeyPosS, which employs True-Range Multilateration, surpassing the previous one-hot and two-hot decoding approaches. The right side visualizes the main idea of the True-Range Multilateration algorithm, initially used in GPS systems and now adapted for facial landmark detection.

1 INTRODUCTION

Facial landmark estimation plays a fundamental role in enriching personalized e-commerce interactions [9, 11–13, 40, 46], providing profound insights into nuanced human analysis [4, 20, 49, 55, 56], and honing the precision of biometric recognition techniques [5–8, 10, 19, 22, 23, 30, 31].

Despite some progress [2, 39, 41], the previous methods heavily rely on heatmap [3, 25, 39, 43, 47, 48, 51, 54, 61] or coordinate regression [15, 17, 34, 36, 37, 41, 52, 59] techniques, leading to challenges such as computational burden and quantization errors. Typically, as shown in Figure 1–2, the heatmap-based methods often have quantization errors when heatmaps are downscaled from their original input [39], while large-resolution heatmaps become computationally expensive [43]. Conversely, coordinate regression-based methods attempt to reduce the computational complexity, but always lack the necessary spatial and contextual information, complicating the task due to inherent visual ambiguity [17].

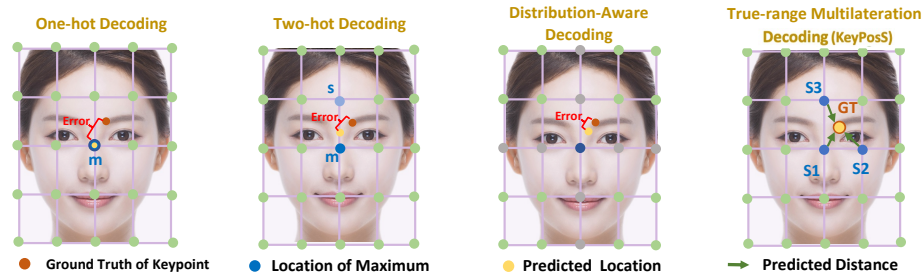


Figure 2: Comparison of four decoding methods: basic one-hot, two-hot, distribution-aware, and our proposed KeyPosS. Despite the inherent "Error" in encoding-decoding, KeyPosS excels with minimal overhead and almost no added computational load.

To address these issues, we present the KeyPoint Positioning System (KeyPosS) — a groundbreaking facial landmark detection paradigm depicted in Figure 4. Uniquely, KeyPosS employs the True-range Multilateration algorithm, initially used in GPS systems, for rapid and accurate facial landmark detection. This framework utilizes a fully convolutional network to predict a distance map, which estimates the distance between a Point of Interest (POI) and multiple anchor points. These anchor points are ingeniously leveraged to triangulate the POI’s position through the True-range Multilateration algorithm. Beyond its strategy, KeyPosS’s plug-and-play nature ensures easy integration into existing models without the need for additional training or modifications. Its usability is further enhanced by its robust location accuracy, even with low-resolution distance maps, making it a versatile and adaptable solution for the challenges in facial landmark detection. To sum up, the invention of KeyPosS revolves around five key aspects:

- (1) *Optimizing heatmap potential*: KeyPosS utilizes the True-Range Multilateration algorithm to analyze both the main response and its neighboring anchor points on the heatmap. This dual principle improves accuracy in intricate scenarios like occlusions or limited visibility.
- (2) *Fusing regression and classification*: KeyPosS classifies POIs and anchors by regressing Gaussian-encoded distances. These dual-purpose tasks effectively represent distances and key points (POIs), thereby streamlining allocation.
- (3) *Robust localization via Station Anchor Sampling*: KeyPosS utilizes regional maxima and neighboring points, enhancing detection robustness and countering errors from isolated peak values.
- (4) *Plug-in Manner for heatmap methods*: The KeyPosS decoding scheme can conveniently retrofit existing heatmap-based methods, promoting adaptability and compatibility across various systems.
- (5) *Improved performance across resolutions*: KeyPosS exhibits better accuracy across varying distance map resolutions, underscoring its flexibility for diverse real-world contexts.

In essence, KeyPosS sets a new benchmark for 2D landmark detection, surpassing contemporary techniques in versatility, scalability, and performance. This enhancement heralds its potential applicability in myriad 2D keypoint use cases, like sports analytics, strengthening their real-time efficiency and robustness.¹

¹The source code is available at <https://github.com/zhiqic/KeyPosS>

2 RELATED WORK

Facial landmark detection has been broadly studied [1, 14, 21, 38, 60]. Particularly, current researches have shifted towards deep learning-based methods, which can be briefly classified into heatmap and coordinate strategies.

Heatmap-based methods. These methods achieve accurate localization and impressive performance by leveraging high-resolution feature maps. The representative architectures like Stacked Hourglass Network [39] and UNet [43] have excelled in this domain [3, 25, 39, 43, 47, 48, 51, 54, 61]. HRNet [47], for instance, obtains high-resolution maps through multi-scale image feature fusion, demonstrating promising results. HSLE [61] proposes a hierarchical structure for accurate alignment, while previous work [39] compensates for quantization error. Darkpose [54] contemplates the heatmap distribution for more precise target locations, and PIPNet [25] performs simultaneous predictions, reducing latency. However, these methods’ heavy reliance on high-resolution feature maps inevitably increases computational costs.

Coordinate regression methods. These approaches directly map discriminative features to target landmark coordinates [15, 17, 34, 36, 37, 41, 52, 59]. For example, DeCaFA [15] integrates U-Net [43] to preserve spatial resolution in cascaded regression for face alignment. Lv et al. [37] introduce Two-Stage Reinitialization (TSR), a deep regression architecture that addresses initialization with a two-stage process, involving global and local stages for coarse and fine alignment. LAB [52] combines heatmap regression with coordinate prediction, employing facial boundaries as geometric constraints. A cascaded Graph Convolutional Network [34] leverages both global and local features for accuracy. Additionally, Nibali et al. [41] propose a differentiable spatial to numerical transform (DSNT) to address differentiation challenges in regression-based methods, ensuring spatial generalization.

Comparison with previous works. KeyPosS is a one-of-a-kind system that stands out for its implementation of GPS-inspired True-Range Multilateration for Point of Interest (POI) localization. Unlike earlier methods that rely solely on regression or classification, KeyPosS seamlessly combines the regression and classification techniques, providing a holistic solution to facial landmark detection. The unique design of KeyPosS allows integration without necessitating modifications, heralding a new era in facial landmark detection. Not only does it offer technical brilliance, but its adaptability ensures that the model is amenable to a variety of applications, which is a marked enhancement over existing methodologies.

3 METHODOLOGY

To better understand our proposed KeyPosS framework, we first review the encoding and decoding methods for facial landmark detection (Sec. 3.1). Following in Sec. 3.2, we first theoretically explore the impact of different keypoint representations, analyzing the quantization error causes of various encoding-decoding schemes. In Sec. 3.3, we also experimentally analyze the error upper bounds when different heatmap resolutions are used as the final output. Finally, Sec. 3.4 presents a comprehensive description of our proposed KeyPosS framework.

3.1 Review of Facial Landmark Detection

Facial landmark detection entails locating predefined landmarks on a human face within an image $I \in \mathbb{R}^{H \times W \times 3}$. The heatmap-based detection pipeline can be defined as:

$$\mathcal{H} = \mathcal{F}(I, W) \quad (1)$$

where \mathcal{F} is the ConvNet backbone, \mathcal{H} is the predicted heatmap, and W is the backbone weight. $\mathcal{H} \in \mathbb{R}^{h \times w \times K}$, with $h = H/\lambda$, $w = W/\lambda$, and λ as the downsampling ratio. K denotes the number of predefined facial landmarks. Generally, joint coordinate prediction involves finding the maximal activation location, but since the heatmap usually doesn't share the original image's spatial size, the heatmaps must be up-sampled using a sample-specific factor λ . This gives rise to a sub-pixel localization problem, typically solved through encoding-decoding pipelines. Gaussian encoding is a common encoding scheme encoding the distance from the point of interest (POI) to the station anchor. We will discuss prior encoder and decoder methods in separate subsections.

3.1.1 Previous Encoding Methods. Traditional encoding strategies can be divided into the following two categories:

(1) *Unbiased Coordinate Encoding.* To address noise from distant station anchors, unbiased coordinate encoding is widely used in previous works. After transforming the ground-truth distances between the station anchors and the POIs, the resolution reduction is defined as:

$$\beta = \frac{\beta}{\lambda} = \left(\frac{u}{\lambda}, \frac{v}{\lambda} \right). \quad (2)$$

Next a spatially variant Gaussian function $\mathcal{G}(\cdot)$ and parameter σ are used to encode the distance. Given a station anchor at (x, y) in the heatmap, the distance encoding $\mathcal{G}(x, y, \beta)$ is defined as:

$$\mathcal{G}(x, y, \beta) = \frac{1}{2\pi\sigma} \exp\left(-\frac{(x-u)^2 + (y-v)^2}{2\sigma^2}\right). \quad (3)$$

The motivation behind this is that this method decreases the distance map's sensitivity to station anchors that are far from the POI, providing more accurate distance predictions.

(2) *Biased Coordinate Encoding.* Different from the previous unbiased coordinate encoding, biased coordinate encoding simply considers the heatmap ground truths as a category label, applying quantization during label assignment as:

$$\beta = \text{Quan}\left(\frac{\beta}{\lambda}\right) = \text{Quan}\left(\left(\frac{u}{\lambda}, \frac{v}{\lambda}\right)\right) \quad (4)$$

where Quan signifies the quantization operation, and the representation is also encoded by Equation 3.

Table 1: Experimental quantization error at different scales of the heatmap. The evaluation metric is Normalized Mean Error (NME, the smaller the better).

Resolution	64 ²	32 ²	16 ²	8 ²	4 ²
One-hot	0.018	0.036	0.071	0.140	0.290
Two-hot [39]	0.009	0.018	0.037	0.090	0.271
Distribution-Aware [54]	0.000	0.001	0.015	0.112	0.289
KeyPosS (Our)	0.000	0.000	0.000	0.000	0.000

3.1.2 Previous Decoding Methods. Common decoding schemes such as One-hot, Two-hot, and Compensation, are outlined here based on the predicted heatmap \mathcal{H} :

(1) *One-hot Decoding.* This strategy identifies the maximum response in \mathcal{H} :

$$\mathbf{m} = \text{argmax}(\mathcal{H}), \quad (5)$$

where \mathbf{m} is the location of the maximum value. The predicted keypoint $\hat{\beta} = \mathbf{m}$.

(2) *Two-hot Decoding.* An enhanced version of One-hot decoding is Two-hot encoding [39], which uses both the first and second maximum value of heatmap \mathcal{H} :

$$\hat{\beta} = \mathbf{m} + 0.25 \frac{\mathbf{m} - \mathbf{s}}{\|\mathbf{m} - \mathbf{s}\|_2}, \quad (6)$$

where $\hat{\beta}$ is the Two-hot decoding result, and \mathbf{s} represents the second maximum value's location. $\|\cdot\|_2$ is the vector magnitude.

(3) *Distribution-aware Decoding.* While the two-hot decoding method accounts for the second maximum response, the target position can't be precisely identified with just two points. The Darkpose approach [54] examines the predicted heatmap's distribution structure to infer the underlying precision location:

$$\mathcal{G}(\beta, \mathbf{x}, \Sigma) = \frac{1}{2\pi r} \exp\left(-\frac{1}{2}(\mathbf{x} - \beta)^T \Sigma^{-1}(\mathbf{x} - \beta)\right), \quad (7)$$

where \mathbf{x} is a pixel location in the predicted heatmap, $\hat{\beta}$ is the Gaussian mean (center) corresponding to the estimated joint location, and the covariance Σ is a diagonal matrix. The objective is to estimate the location β . The precision location can be approximated by evaluating a Taylor series (up to the quadratic term) at the maximal activation m of the predicted heatmap. The details can be found in [54]. The final equation is as follows:

$$\hat{\beta} = D'(m) + D''(m), \quad (8)$$

where D' and D'' represent the first and second-order derivatives of the predicted heatmap, respectively.

3.2 Theoretical Quantization Error

After a brief review of different encoding and decoding approaches, we explore various keypoint decoding strategies, including one-hot and two-hot heatmaps, the distribution-aware method, and our KeyPosS method (shown in Figure 2). Our goal is to analyze their technical characteristics and understand the underlying mechanisms that contribute to quantization error.

(1) **One-Hot Decoding.** This technique is similar to traditional object detection methods and quantizes keypoint coordinates based on the heatmap resolution. The argmax operation selects the highest value as the keypoint location, which can result in notable errors due to misalignment between the ground truth location and the maximum response, especially when the downsampling ratio

increases. The theoretical error can be estimated as half of the resolution’s grid size.

(2) Two-hot Decoding. Building upon the one-hot strategy, the two-hot approach includes both the maximum and second maximum responses in the prediction. This mitigates some of the localization error by providing a refined representation, but the quantization error may still be substantial. The incorporation of two maximum responses can offer a better approximation, but it does not fully overcome the discretization nature of the heatmap.

(3) Distribution-Aware Decoding: The distribution-aware decoding strategy, proposed by Zhang et al. [54], reduces localization error by evaluating the Taylor series around the maximum activation position. This method considers the trends of neighboring points, providing an approximation that counters the discrete nature of heatmaps. The theoretical insight is that by taking into account the continuous distribution of the underlying data, the strategy becomes more robust with high-resolution heatmaps but suffers with low-resolution ones.

(4) Our KeyPosS. Our proposed KeyPosS is a distance map-based heatmap that calculates the distance from a fixed anchor to the point of interest (POI). It employs True-range Multilateration to overcome the limitations of one-hot and two-hot techniques, resulting in more accurate localization. The method’s accuracy is based on precise distance predictions, which produce dependable and accurate results across a variety of heatmap resolutions.

Insights into Quantization Error. Quantization error in these methods is fundamentally linked to discretization of the continuous space and the argmax operation used in decoding. Figure 3 illustrates that upsampling can exacerbate these errors. Strategies like two-hot [39] and distribution-aware decoding [54] alleviate errors, but low-resolution heatmaps can still cause significant performance degradation.

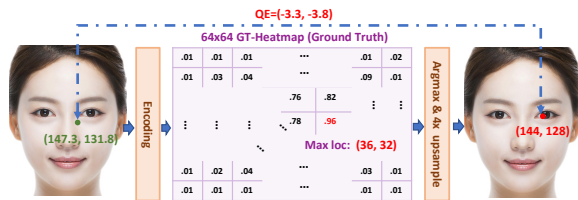


Figure 3: Unveiling the Theoretical Quantization Error Induced by the One-Hot (Argmax) Decoding Scheme. The term "QE" denotes the quantization error, and the "GT-heatmap" represents the heatmap encoded by the ground truth coordinate. This diagram illustrates how the upsampling step can amplify these errors, especially in smaller heatmap resolutions, and highlights that methods like two-hot and distribution-aware decoding provide alleviation but are not immune to significant performance degradation with low-resolution heatmaps.

3.3 Experimental Quantization Error

After a rough intuitive theoretical analysis, we experimentally analyze quantization errors in multi-keypoint decoding strategies across different heatmap sizes. Table 1 details the experiment that uses GT keypoint coordinates as input. We evaluate the Normalized Mean Error (NME) between predicted and actual coordinates. Specifically, our analysis leverages the unbiased encoding method

compatible with prevalent decoding techniques such as one-hot, two-hot, and distribution-aware.

(1) One-hot & Two-hot Decoding. These decoding approaches demonstrate significant performance degradation as the heatmap scale decreases. While they may provide acceptable accuracy in high-resolution scenarios, the quantization error becomes more pronounced in low-resolution contexts, confirming the previous theoretical observations.

(2) Distribution-Aware Decoding. Acting as a compensation strategy, the distribution-aware decoding outperforms one-hot decoding at higher resolutions but experiences a sharp drop in performance under low-resolution conditions. This behavior emphasizes its ability to correct some errors in high-resolution settings, but also exposes its limitations when resolution is reduced.

(3) Our KeyPosS. Our proposed KeyPosS strategy, employing a multilateration method, showcases impressive robustness and adaptability across various heatmap scales. By interpreting the heatmap as a fusion of label and distance, it is able to shift seamlessly between high-resolution compensation-based methods and regression-based methods. This innovative approach transcends the boundaries of traditional strategies, suggesting that KeyPosS could provide a broader solution for different scenarios.

Summary of Experimental Analysis. The experimental results elucidate the complex relationship between heatmap scale, decoding strategies, and resulting quantization errors. In general, the results of the experimental analysis resonate with the theoretical analysis, shedding light on the specific strengths and weaknesses of each method in real-world applications. Notably, the consistent performance of our KeyPosS across different scales highlights its potential as a groundbreaking approach in keypoint representation.

3.4 Crafting KeyPosS Framework

Our KeyPosS approach, visualized in Figure 4, comprises several stages. Initially, an input image is processed through HRNet [47] to extract relevant features. Subsequently, a keypoint prediction head generates a distance map encoding the distance between the Point of Interest (POI) and station anchors. Formally, given an input image I , the backbone network $\mathcal{F}(\cdot)$ computes the feature map f , $f \in R^{H \times W \times C}$, using the network weights W . From this feature map, the keypoint prediction head constructs the final heatmap $\mathcal{H} \in R^{H \times W \times K}$.

(1) Distance Encoding Model. HRNet’s high-resolution architecture [47] has been effective in dense label prediction tasks. However, to adapt to memory bandwidth constraints in mobile and edge devices, we propose a lightweight version of HRNet, which employs early fast downsampling. This downsampling uses convolutional layers with a fixed 3×3 kernel size. Tab.2 shows the configurations for the number and stride of the convolutional layer.

(2) Station Anchor Sampling Strategy. The accuracy of the POI location prediction hinges on an appropriate selection of station anchors. These are chosen based on two criteria: a) selection of over three non-collinear anchors and b) prediction accuracy decreases as distance increases.

To meet these requirements, we propose a filtering-based anchor sampling strategy. For a given heatmap \mathcal{H} , we apply a fixed filter kernel K to the original heatmap using the operation \otimes , which is

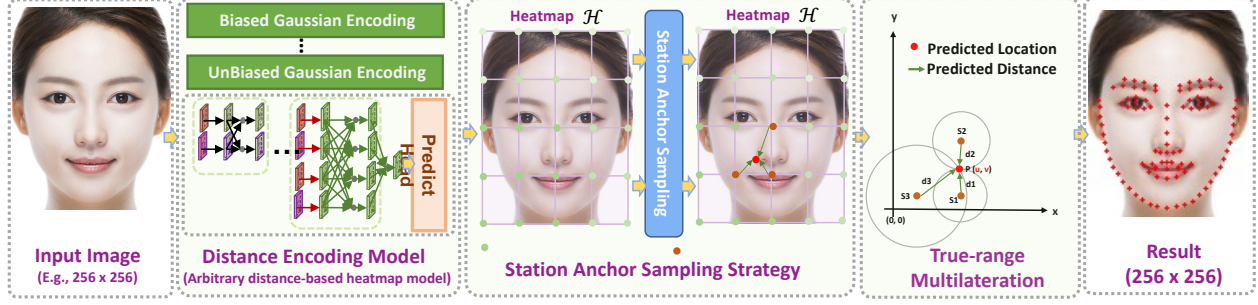


Figure 4: The pipeline of the proposed KeyPosS, consists of three components: (1) Distance Encoding Model, (2) Station Anchor Sampling Strategy, and (3) True-range Multilateration. The KeyPosS scheme is versatile and can be adopted in *any distance encoding-based approach*.

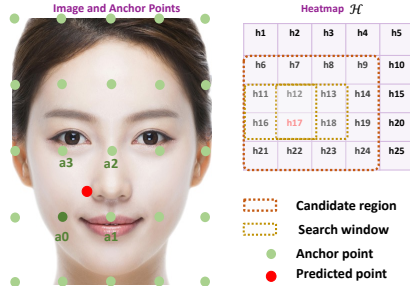


Figure 5: Strategy of Anchor Sampling: A 5×5 heatmap illustrating the selection of the highest response points (e.g., h12, h13, h17, h18) within a search window centered around h17. The orange dashed box represents the search window, which is slid with a step size of 1, ensuring non-collinearity and optimizing the Normalized Mean Error (NME) using 3 or 4 anchor points.

performed with a stride of 1 and a kernel value of 1. We then find the region in the input-filtered heatmap with the highest value, which is used in the True-range Multilateration algorithm. By adjusting the kernel size, we can control the number of sampled anchors, ensuring their non-collinearity.

As shown in Figure 5, consider a 5×5 heatmap. The process begins by finding the point on the heatmap with the highest value, such as point h17. A search window of range $[-2, +2]$ is centered around h17 (shown by the orange dashed box). This window is slid with a step size of 1 to find the four points with the highest responses, which might be points h12, h13, h17, and h18, as anchor points for decoding. This method ensures non-collinearity of the selected anchor points. Experimental results show that the Normalized Mean Error (NME) is minimized with 3 or 4 anchor points.

(3) True-range Multilateration. The True-range Multilateration algorithm is widely employed in various positioning applications. Given a set of station anchors $\mathcal{A} = \{A(x_0, y_0), A(x_1, y_1), \dots, A(x_n, y_n)\}$ and their corresponding distances $\mathcal{D} = \{d_0, d_1, \dots, d_n\}$ to the POI \mathbf{p} , a system of non-linear equations is formulated as follows:

$$\begin{cases} (x_0 - u)^2 + (y_0 - v)^2 = d_0^2 \\ (x_1 - u)^2 + (y_1 - v)^2 = d_1^2 \\ \vdots \\ (x_n - u)^2 + (y_n - v)^2 = d_n^2 \end{cases} \quad (9)$$

Table 2: Setup of convolutional layers for expedited downsampling. The symbol ‘-’ denotes the absence of a specific convolutional layer.

Resolution	64	32	16	8	4
Conv1.Stride	2	4	4	4	4
Conv2.Stride	2	2	4	4	4
Conv3.Stride	-	-	-	2	2
Conv4.Stride	-	-	-	-	2

where x_n , y_n , and d_n denote the x , y coordinates of the station anchor $A(x_n, y_n)$ and the distance from the station anchor to the POI \mathbf{p} . The system of non-linear equations can be solved using the least square method, which is transformed into the form:

$$\mathbf{Y} = \hat{\beta} \mathbf{X} \quad (10)$$

In this equation, $\hat{\beta}$ represents the POI location to be estimated, and \mathbf{X} , \mathbf{Y} , and $\hat{\beta}$ are defined as follows:

$$\mathbf{X} = \begin{bmatrix} x_n - x_1 & y_n - y_1 \\ x_n - x_2 & y_n - y_2 \\ \vdots \\ x_n - x_{n-1} & (y_n - y_{n-1}) \end{bmatrix} \quad (11)$$

$$\mathbf{Y} = \begin{bmatrix} (d_1^2 - d_n^2 + x_n^2 + y_n^2 - x_1^2 - y_1^2)/2 \\ (d_2^2 - d_n^2 + x_n^2 + y_n^2 - x_2^2 - y_2^2)/2 \\ \vdots \\ (d_{n-1}^2 - d_n^2 + x_n^2 + y_n^2 - x_{n-1}^2 - y_{n-1}^2)/2 \end{bmatrix} \quad (12)$$

$$\hat{\beta} = \begin{bmatrix} u \\ v \end{bmatrix} \quad (13)$$

The predicted location $\hat{\beta}$ can be obtained by:

$$\hat{\beta} = (\mathbf{X}^T \mathbf{X})^{-1} \mathbf{X}^T \mathbf{Y} \quad (14)$$

(4) Training Details. KeyPosS utilizes Mean Square Error (MSE) loss [17] for supervising model training. The MSE loss is calculated as follows:

$$\mathcal{L} = \sum_{i=1}^K \|\beta_i - \hat{\beta}_i\|_2 \quad (15)$$

where β_i and $\hat{\beta}_i$ represent the ground truth and predicted locations, respectively, with $\hat{\beta}_i$ computed using Equation 14, and K representing the total facial landmarks. The model, during training, uses face images and Ground Truth (GT) heatmaps - encoded from GT coordinates - as input and produces a set of heatmaps. While HRNet was the model in our experiments, other suitable models

Table 3: Comparison with the State-of-the-Art methods. The results are in NME (%). The best results are highlighted with bold text font.

Method	Year	Pretrained	WFLW [52]	AFLW [28]	300W [45]	Parameters	GFlops
DAC-CSR [18]	CVPR2017	-	-	2.27	-	-	-
TSR [36]	CVPR2017	-	-	2.17	4.99	-	-
LAB [52]	CVPR2018	-	5.27	1.85	3.49	24.1M+28.3M	26.7+2.4
Wing [17]	CVPR2018	Y	4.99	1.47	-	91.0M	5.5
ODN [58]	CVPR2019	Y	-	1.63	4.17	-	-
DeCaFa [15]	ICCV2019	-	4.62	-	3.39	10M	-
DAG [35]	ECCV2020	Y	4.21	-	3.04	-	-
AWing [51]	ICCV2019	N	4.36	1.53	3.07	24.1M	26.7
AVS [42]	ICCV2019	N	4.39	-	3.86	28.3M	2.4
ADA [3]	CVPR2020	-	-	-	3.50	-	-
LUVLi [29]	CVPR2020	N	4.37	1.39	3.23	-	-
PIPNet-18 [25]	IJCV2021	Y	4.57	1.48	3.36	12.0M	2.4
PIPNet-101 [25]	IJCV2021	Y	4.31	1.42	3.19	45.7M	10.5
DTLD [32]	CVPR2022	Y	4.08	1.38	2.96	-	-
RePFormer [33]	IJCAI2022	Y	4.11	1.43	3.01	-	-
SLPT [53]	CVPR2022	-	4.14	-	3.17	9.98M	-
EF-3-ACR [16]	ICPR2022	-	-	-	3.75	-	-
ADNet-FE5 [24]	AAAI2022	Y	4.1	-	2.87	-	-
ResNet50-FE5 [24]	AAAI2022	-	-	-	4.39	-	-
HRNet-FE5 [24]	AAAI2022	-	-	-	3.46	-	-
STAR Loss [57]	CVPR2023	-	4.02	-	2.87	13.37M	-
RHT-R [50]	TIP2023	-	4.01	1.99	3.46	-	-
KeyPosS (Biased)	2023	Y	4.0	1.35	3.39	9.7M	4.7
KeyPosS (Unbiased)	2023	Y	4.0	1.35	3.34	9.7M	4.7

can be utilized. The JointsMSELoss function, calculated between the predicted and GT heatmap, is employed as the loss function.

The training employs Adam optimizer, linear-step learning rate, and a batch size of 64×64 for 100 to 1000 epochs. The input image size is $256 \times 256 \times 3$, and the output heatmap size is $K \times H \times W$, where K is the number of keypoints, and H and W are the height and width of the heatmap image (values such as 64, 32, 16, 8, 4), respectively. We evaluated the model’s performance using Normalized Mean Error (NME) as the metric, training models with varying heatmap sizes (64, 32, 16, 8, 4) on numerous open-source face datasets and testing on the corresponding test datasets.

4 EXPERIMENTS

We first present the dataset and evaluation metrics (Sec. 4.1), followed by detailing the implementation of our KeyPosS (Sec. 4.2). Subsequently, we compare our approach with state-of-the-art methods (Sec. 4.3) and prior decoding techniques (Sec. 4.4). Finally, we offer ablation studies (Sec. 4.5), visual results (Sec. 4.6), and an efficiency analysis (Sec. 4.7).

4.1 Dataset and Metric

WFLW [52]. The Wider Facial Landmarks in-the-wild (WFLW) dataset includes 10,000 face images (7,500 for training and 2,500 for testing), each annotated with 98 landmarks. With substantial pose, expression, and occlusion variations, the test set is further divided into six evaluation categories: pose, expression, illumination, make-up, occlusion, and blur.

AFLW [28]. The Annotated Facial Landmarks in the Wild (AFLW) dataset provides a large-scale collection of annotated face images from Flickr. These images display extensive variation in appearance (e.g., pose, expression, ethnicity, age, gender) and general imaging

and environmental conditions. Overall, approximately 25k faces are annotated, with up to 21 landmarks per image.

300W [45]. The 300W dataset comprises 300 indoor and 300 outdoor in-the-wild images, covering a wide range of identities, expressions, illumination conditions, poses, occlusion, and face sizes. Notably, each face in the dataset is annotated with 68 landmarks.

COCO-WholeBody [26]. The COCO-WholeBody dataset extends the COCO dataset with whole-body annotations. It features four types of bounding boxes (person, face, left-hand, right-hand) and 133 keypoints (17 body, 6 feet, 68 face, 42 hands) per person in an image. In this study, we only focus on face landmarks annotation for performance evaluation.

Evaluation Metric. For consistency with previous works, we adopt the Normalized Mean Error (NME) metric to evaluate our model. Typically, it is calculated as follows:

$$\mathcal{L} = \sum_{i=1}^N \|\beta_i - \hat{\beta}_i\|_2 \quad (16)$$

where β and $\hat{\beta}$ represent the ground truth and predicted results, respectively. D denotes the normalized distance, and N is the number of landmarks.

4.2 Implementation Details

We train the proposed KeyPosS model end-to-end for 100 epochs using the Adam optimizer [27]. An HRNet pre-trained on ImageNet [44] serves as the initial backbone. The learning rate starts at $2e-3$, reducing to $1e-5$ at the 100th epoch, with a batch size of 64. We implement our method using the MMpose keypoint detection toolbox². All experiments are conducted on a server equipped with 4 NVIDIA V100 GPUs. For all datasets, faces are cropped based

²<https://github.com/open-mmlab/mmpose>

on the provided bounding boxes and resized to 256×256 . Data augmentation techniques, such as translation, random horizontal flipping, random rotation, and random scaling, are applied.

4.3 Comparison with the State-of-the-Art

Table 3 shows KeyPosS against state-of-the-art methods on four key datasets. On AFLW and WFLW, KeyPosS stands out, superior to one-hot and two-hot heatmap-based baselines, by considering neighboring responses to correct maximum response location. Meanwhile, coordinate regression-based techniques fall behind, as they often lose spatial details during forward passes, hindering high-precision localization. KeyPosS’s amalgamation of classification and regression excels here, particularly in high-resolution settings.

On the 300W dataset, KeyPosS’s performance (3.39% NME) highlights two challenges: 1) the complexity of the 300W dataset and 2) under-fitting due to limited training data. While acknowledging DTLT’s impressive performance on the same, KeyPosS’s competitive results on WFLW and AFLW with fewer parameters and higher computational efficiency must not be overlooked.

The results on the COCO-WholeBody dataset, presented in Table 5, further support KeyPosS’s proficiency. Since recent works lack experiments on this dataset, a direct comparison is elaborated in our ablation studies.

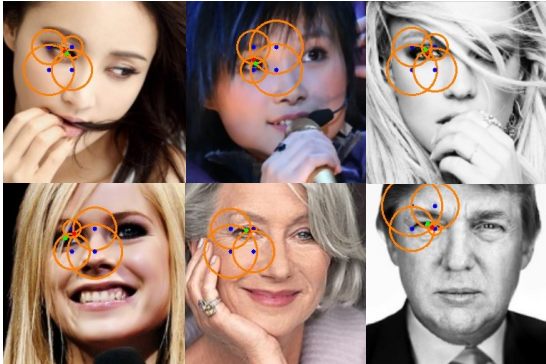


Figure 6: True-range Multilateration depicted visually. The blue, green, and red dots indicate the anchor station, actual position, and predicted location respectively. Predicted distances are represented by orange circles.

Table 4: Impact of Anchor Sampling on Model Performance.

Kernel size	2×2	3×3	4×4	5×5	6×6
64^2	4.00	4.00	3.98	3.99	3.99
32^2	4.30	4.29	4.27	4.28	4.30
16^2	4.94	4.94	4.95	4.96	5.00
8^2	7.67	7.69	7.72	7.80	9.41
4^2	12.04	26.57	18.74	-	-

4.4 Comparison with Decoding Schemes

KeyPosS is a plug-in decoding scheme that can be easily incorporated into existing encoding methods. To validate its effectiveness and robustness, we adopt two classic biased and unbiased encoding strategies (employed in DarkPose [54]), benchmarking against one-hot, two-hot, and distribution-aware decoding baselines. The upper part of the Table 5 shows results for *Biased Encoding*, following the original one-hot/two-hot methods, while the bottom part demonstrates results for *Unbiased Encoding*.

KeyPosS outperforms one-hot and two-hot methods across all resolutions on COCO-WholeBody, WFLW, and AFLW, as per the biased encoding results. Notably, KeyPosS achieves significant improvements in the resolution range from 16×16 to 4×4 , highlighting its robustness. Although the two-hot baseline yields reasonable performance in high-resolution heatmaps, it still lags behind KeyPosS, demonstrating the superiority of KeyPosS over the relatively simplistic two-hot approach.

The results with unbiased encoding largely mirror those of biased encoding. KeyPosS, however, holds its own against distribution-aware methods in 64×64 and 32×32 resolutions. These results reveal some of KeyPosS’s limitations, such as its heavy dependence on distance prediction accuracy. The True-range Multilateration problem cannot be precisely solved using the least squares process, and the predicted heatmap can contain multiple peaks, leading to incorrect solutions - areas for future research.

4.5 Ablation Studies

Effect of Anchor Sampling. To understand the influence of the stationary anchor sampling strategy, we performed ablation studies focusing on kernel size and heatmap resolution. The results, as illustrated in Table 4, confirm that a small 2×2 kernel size delivers optimal performance across varying resolutions. This discovery underscores the significance of focusing on the highest response region for precise localization. Interestingly, it also suggests that simply increasing the number of stationary anchors does not lead to corresponding enhancements in performance.

Exploration of True-range Multilateration. A comprehensive analysis of True-range Multilateration’s role in localization was conducted by visualizing the distance predictions and their intersecting regions. As shown in Table 4, the investigation revealed that location errors are primarily attributed to inaccuracies in distance prediction. Generally, a shorter span from the stationary anchor results in more precise distance approximations. However, as illustrated in Figure 6, even the proximity of the closest anchor can introduce substantial errors. This highlights that stationary anchor sampling, while critical to our method, still poses significant challenges and offers opportunities for further refinement.

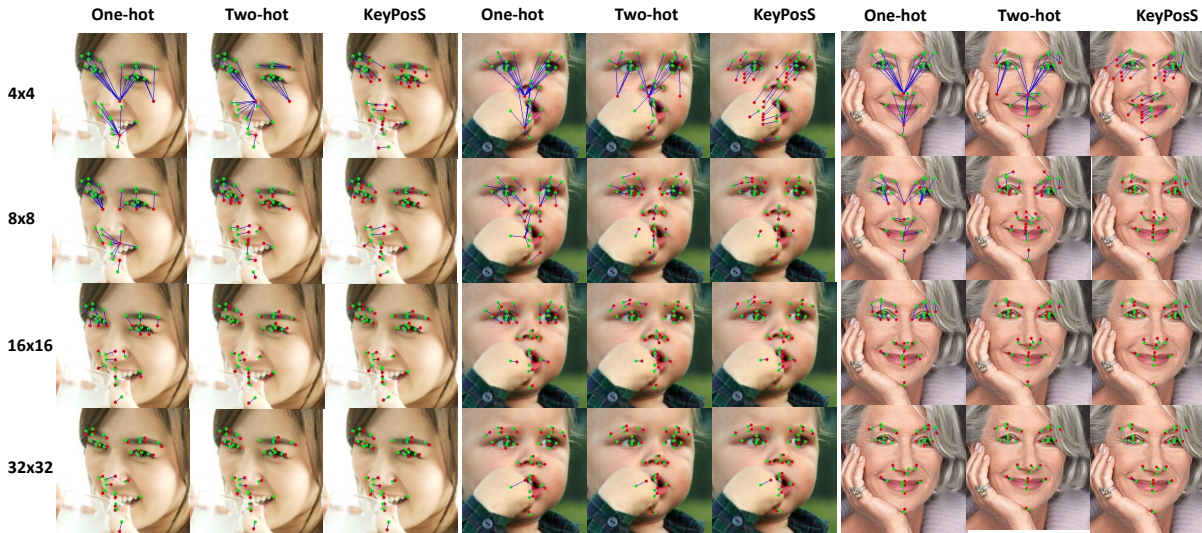
4.6 Visualization Analysis

To delve deeper into the adaptability of proposed KeyPosS, particularly in real-world applications, we undertook visualization analysis to comprehensively study its performance. The experiments included comparative assessments with one-hot and two-hot baselines. Since the existing methods already demonstrate acceptable results in high-resolution heatmap configurations, our focus shifted to the more challenging low-resolution settings. These comparisons are visually depicted in Figure 7.

Upon examination, it is clear that the traditional one-hot and two-hot frameworks falter at lower resolutions, such as 4×4 and 8×8 , failing to provide accurate predictions. In contrast, our proposed KeyPosS maintains functionality even at the 4×4 resolution and excels at 8×8 and higher resolutions. A significant observation is that when the resolution exceeds 32×32 , the predicted results across various methods converge, becoming virtually indistinguishable. This finding underscores the impressive capabilities of KeyPosS, proving its effectiveness not only at low resolutions but

Table 5: Performance of keypoint representations at different scales of the heatmap.

Dataset	WFLW [52]					AFLW [28]					COCO-WholeBody [26]				
	64 ²	32 ²	16 ²	8 ²	4 ²	64 ²	32 ²	16 ²	8 ²	4 ²	64 ²	32 ²	16 ²	8 ²	4 ²
One-hot	4.28	5.23	7.59	14.74	28.8	1.57	2.11	3.57	6.52	13.06	5.96	7.14	10.50	17.98	37.7
Two-hot [39]	4.06	4.55	5.83	12.3	27.4	1.41	1.66	2.54	5.08	12.77	5.59	6.08	8.11	14.28	34.54
KeyPosS (Biased)	3.99	4.30	5.03	9.96	19.48	1.35	1.49	2.12	4.18	10.04	5.45	5.64	6.93	10.98	27.85
Distribution-Aware [54]	3.96	4.25	5.38	11.83	26.05	1.35	1.43	1.77	4.83	13.28	5.10	5.71	6.58	15.71	40.12
KeyPosS (Unbiased)	3.98	4.27	4.94	7.68	12.04	1.35	1.43	1.73	3.34	4.54	5.17	5.80	6.19	10.37	27.59

**Figure 7: Depiction of heatmap size’s influence on prediction outcomes. Results are shown at varying heatmap scales, in descending order. One-hot, two-hot, and KeyPosS prediction results are grouped separately. Ground truth is represented by green dots, and predicted results by red dots. Discrepancies between predictions and ground truth are highlighted with blue lines.****Table 6: Efficiency at Different Scale.**

input size	256 × 256				
heatmap size	64 ²	32 ²	16 ²	8 ²	4 ²
Flops(GFLOPs)	4.75	1.19	0.3	0.07	0.03
Params(M)	9.74	9.74	9.74	9.66	9.64

also in scenarios requiring standard precision. This visualization analysis further accentuates the innovative nature of KeyPosS and its substantial potential in a wide array of applications.

4.7 Efficiency at Different Heatmap Scales

The KeyPosS exhibits robust performance across various heatmap resolutions, thereby demonstrating its adaptability and efficiency. By conducting a thorough efficiency analysis using different resolution scales, we discovered that the downsampling of the feature map executed before the first stage of HRNet leads to an exponential reduction in FLOPs without a corresponding drop in performance quality. Notably, as shown in Table 6, KeyPosS maintains impressive functionality even at lower resolutions such as 16 × 16 and 8 × 8. In practical applications, these resolution settings correspond to a mere 0.3 and 0.07 GFlops, respectively. Such low computational requirements highlight the potential of KeyPosS as an exceptionally lightweight solution for facial landmark detection. This key feature renders it a valuable asset in real-world scenarios where computational resources might be scarce or constrained.

5 CONCLUSION

We introduced KeyPosS, an innovative face landmark detection framework that incorporates the True-range Multilateration algorithm, commonly used in GPS systems, to pinpoint Points of Interest (POIs) in 2D images. By deploying a fully convolutional network, KeyPosS generates a distance map from POIs to designated anchor points, then triangulates the POIs’ precise location. When benchmarked against leading models across diverse datasets, KeyPosS showcased superior performance and efficiency. Its prowess positions it as a breakthrough in facial landmark detection, especially in resource-constrained or low-resolution contexts. Future endeavors will widen KeyPosS’s application to encompass object detection and pose estimation.

ACKNOWLEDGMENTS

The contributions of Zhi-Qi Cheng in this project were supported by the Army Research Laboratory (W911NF-17-5-0003), the Air Force Research Laboratory (FA8750-19-2-0200), the U.S. Department of Commerce, National Institute of Standards and Technology (60NANB17D156), the Intelligence Advanced Research Projects Activity (D17PC00340), and the US Department of Transportation (69A3551747111). Intel and IBM Fellowships also provided additional support for Zhi-Qi Cheng’s research work. The views and conclusions contained herein represent those of the authors and not necessarily the official policies or endorsements of the supporting agencies or the U.S. Government.

REFERENCES

- [1] Xudong Cao, Yichen Wei, Fang Wen, and Jian Sun. 2014. Face Alignment by Explicit Shape Regression. *International Journal of Computer Vision* 107, 2 (2014), 177–190.
- [2] Zhe Cao, Gines Hidalgo, Tomas Simon, Shih-En Wei, and Yaser Sheikh. 2021. OpenPose: Realtime Multi-Person 2D Pose Estimation Using Part Affinity Fields. *IEEE Transactions on Pattern Analysis and Machine Intelligence* 43, 1 (2021), 172–186.
- [3] Prashanth Chandran, Derek Bradley, Markus H. Gross, and Thabo Beeler. 2020. Attention-Driven Cropping for Very High Resolution Facial Landmark Detection. In *IEEE Conference on Computer Vision and Pattern Recognition*.
- [4] Hanyuan Chen, Jun-Yan He, Wangmeng Xiang, Wei Liu, Zhi-Qi Cheng, Hanbing Liu, Bin Luo, Yifeng Geng, and Xuansong Xie. 2023. HDFormer: High-order Directed Transformer for 3D Human Pose Estimation. *arXiv preprint arXiv:2302.01825* (2023).
- [5] Zhi-Qi Cheng, Qi Dai, Hong Li, Jingkuan Song, Xiao Wu, and Alexander G Hauptmann. 2022. Rethinking spatial invariance of convolutional networks for object counting. In *IEEE/CVF Conference on Computer Vision and Pattern Recognition*. 19638–19648.
- [6] Zhi-Qi Cheng, Qi Dai, Siyao Li, Teruko Mitamura, and Alexander Hauptmann. 2022. Gsrformer: Grounded situation recognition transformer with alternate semantic attention refinement. In *ACM International Conference on Multimedia*. 3272–3281.
- [7] Zhi-Qi Cheng, Jun-Xiu Li, Qi Dai, Xiao Wu, and Alexander G Hauptmann. 2019. Learning spatial awareness to improve crowd counting. In *IEEE/CVF international conference on computer vision*. 6152–6161.
- [8] Zhi-Qi Cheng, Jun-Xiu Li, Qi Dai, Xiao Wu, Jun-Yan He, and Alexander G Hauptmann. 2019. Improving the Learning of Multi-column Convolutional Neural Network for Crowd Counting. In *ACM International Conference on Multimedia*. 1897–1906.
- [9] Zhi-Qi Cheng, Yang Liu, Xiao Wu, and Xian-Sheng Hua. 2016. Video ecommerce: Towards online video advertising. In *ACM international conference on Multimedia*. 1365–1374.
- [10] Zhi-Qi Cheng, Xiao Wu, Siyu Huang, Jun-Xiu Li, Alexander G Hauptmann, and Qiang Peng. 2018. Learning to transfer: Generalizable attribute learning with multitask neural model search. In *ACM international conference on Multimedia*. 90–98.
- [11] Zhi-Qi Cheng, Xiao Wu, Yang Liu, and Xian-Sheng Hua. 2017. Video ecommerce++: Toward large scale online video advertising. *IEEE transactions on multimedia* 19, 6 (2017), 1170–1183.
- [12] Zhi-Qi Cheng, Xiao Wu, Yang Liu, and Xian-Sheng Hua. 2017. Video2shop: Exact matching clothes in videos to online shopping images. In *IEEE conference on computer vision and pattern recognition*. 4048–4056.
- [13] Zhi-Qi Cheng, Hao Zhang, Xiao Wu, and Chong-Wah Ngo. 2017. On the selection of anchors and targets for video hyperlinking. In *ACM on international conference on multimedia retrieval*. 287–293.
- [14] David Cristinacce and Timothy F. Cootes. 2008. Automatic feature localisation with constrained local models. *Pattern Recognition* 41, 10 (2008), 3054–3067.
- [15] Arnaud Dapogny, Matthieu Cord, and Kevin Bailly. 2019. DeCaFA: Deep Convolutional Cascade for Face Alignment in the Wild. In *IEEE International Conference on Computer Vision*. 6892–6900.
- [16] Ali Pourramezan Fard and Mohammad H Mahoor. 2022. ACR loss: Adaptive coordinate-based regression loss for face alignment. In *International Conference on Pattern Recognition*. IEEE, 1807–1814.
- [17] Zhen-Hua Feng, Josef Kittler, Muhammad Awais, Patrik Huber, and Xiao-Jun Wu. 2018. Wing Loss for Robust Facial Landmark Localisation With Convolutional Neural Networks. In *IEEE Conference on Computer Vision and Pattern Recognition*. 2235–2245.
- [18] Zhen-Hua Feng, Josef Kittler, William J. Christmas, Patrik Huber, and Xiaojun Wu. 2017. Dynamic Attention-Controlled Cascaded Shape Regression Exploiting Training Data Augmentation and Fuzzy-Set Sample Weighting. In *IEEE Conference on Computer Vision and Pattern Recognition*. 3681–3690.
- [19] Jun-Yan He, Zhi-Qi Cheng, Chenyang Li, Wangmeng Xiang, Binghui Chen, Bin Luo, Yifeng Geng, and Xuansong Xie. 2023. DAMO-StreamNet: Optimizing Streaming Perception in Autonomous Driving. *arXiv preprint arXiv:2303.17144* (2023).
- [20] Jun-Yan He, Xiao Wu, Zhi-Qi Cheng, Zhaoquan Yuan, and Yu-Gang Jiang. 2021. DB-LSTM: Densely-connected Bi-directional LSTM for human action recognition. *Neurocomputing* 444 (2021), 319–331.
- [21] Martial Hebert, Katsushi Ikeuchi, and Herve Delingette. 1995. A Spherical Representation for Recognition of Free-Form Surfaces. *IEEE Transactions on Pattern Analysis and Machine Intelligence* 17, 7 (1995), 681–690.
- [22] Siyu Huang, Xi Li, Zhi-Qi Cheng, Zhongfei Zhang, and Alexander Hauptmann. 2018. Gnas: A greedy neural architecture search method for multi-attribute learning. In *ACM international conference on Multimedia*. 2049–2057.
- [23] Siyu Huang, Xi Li, Zhi-Qi Cheng, Zhongfei Zhang, and Alexander Hauptmann. 2020. Stacked pooling for boosting scale invariance of crowd counting. In *IEEE International Conference on Acoustics, Speech and Signal Processing*. IEEE, 2578–2582.
- [24] Yangyu Huang, Xi Chen, Jongyoo Kim, Hao Yang, Chong Li, Jiaolong Yang, and Dongyue Chen. 2023. FreeEnricher: Enriching Face Landmarks without Additional Cost. In *AAAI Conference on Artificial Intelligence*, Vol. 37. 962–970.
- [25] Haibo Jin, Shengcai Liao, and Ling Shao. 2021. Pixel-in-Pixel Net: Towards Efficient Facial Landmark Detection in the Wild. *International Journal of Computer Vision* 12 (2021), 3174–3194.
- [26] Sheng Jin, Lumin Xu, Jin Xu, Can Wang, Wentao Liu, Chen Qian, Wanli Ouyang, and Ping Luo. 2020. Whole-Body Human Pose Estimation in the Wild. In *European Conference on Computer Vision*, Vol. 12354. 196–214.
- [27] Diederik P. Kingma and Jimmy Ba. 2015. Adam: A Method for Stochastic Optimization. In *International Conference on Learning Representations*.
- [28] Martin Köstinger, Paul Wohlhart, Peter M. Roth, and Horst Bischof. 2011. Annotated Facial Landmarks in the Wild: A large-scale, real-world database for facial landmark localization. In *IEEE International Conference on Computer Vision Workshops*. 2144–2151.
- [29] Abhinav Kumar, Tim K. Marks, Wenxuan Mou, Ye Wang, Michael Jones, Anoop Cherian, Toshiaki Koike-Akino, Xiaoming Liu, and Chen Feng. 2020. LUVLi Face Alignment: Estimating Landmarks' Location, Uncertainty, and Visibility Likelihood. In *IEEE Conference on Computer Vision and Pattern Recognition*. 8233–8243.
- [30] Jin-Peng Lan, Zhi-Qi Cheng, Jun-Yan He, Chenyang Li, Bin Luo, Xu Bao, Wangmeng Xiang, Yifeng Geng, and Xuansong Xie. 2023. Procontext: Exploring progressive context transformer for tracking. In *IEEE International Conference on Acoustics, Speech and Signal Processing*. IEEE, 1–5.
- [31] Chenyang Li, Zhi-Qi Cheng, Jun-Yan He, Pengyu Li, Bin Luo, Hanyuan Chen, Yifeng Geng, Jin-Peng Lan, and Xuansong Xie. 2023. Longshortnet: Exploring temporal and semantic features fusion in streaming perception. In *IEEE International Conference on Acoustics, Speech and Signal Processing*. IEEE, 1–5.
- [32] Hui Li, Zidong Guo, Seon-Min Rhee, Seungju Han, and Jae-Joon Han. 2022. Towards Accurate Facial Landmark Detection via Cascaded Transformers. In *IEEE Conference on Computer Vision and Pattern Recognition*. 4166–4175.
- [33] Jinpeng Li, Haibo Jin, Shengcai Liao, Ling Shao, and Pheng-Ann Heng. 2022. Repformer: Refinement pyramid transformer for robust facial landmark detection. *arXiv preprint arXiv:2207.03917* (2022).
- [34] Weijian Li, Yuhang Lu, Kang Zheng, Haofu Liao, Chihung Lin, Jiebo Luo, Chit-Tung Cheng, Jing Xiao, Le Lu, Chang-Fu Kuo, and Shun Miao. 2020. Structured Landmark Detection via Topology-Adapting Deep Graph Learning. In *European Conference on Computer Vision*. 266–283.
- [35] Weijian Li, Yuhang Lu, Kang Zheng, Haofu Liao, Chihung Lin, Jiebo Luo, Chit-Tung Cheng, Jing Xiao, Le Lu, Chang-Fu Kuo, and Shun Miao. 2020. Structured Landmark Detection via Topology-Adapting Deep Graph Learning. In *European Conference on Computer Vision*, Vol. 12354. 266–283.
- [36] Jiang-Jing Lv, Xiaohu Shao, Junliang Xing, Cheng Cheng, and Xi Zhou. 2017. A Deep Regression Architecture with Two-Stage Re-initialization for High Performance Facial Landmark Detection. In *Conference on Computer Vision and Pattern Recognition*. 3691–3700.
- [37] Jiang-Jing Lv, Xiaohu Shao, Junliang Xing, Cheng Cheng, and Xi Zhou. 2017. A Deep Regression Architecture with Two-Stage Re-initialization for High Performance Facial Landmark Detection. In *IEEE Conference on Computer Vision and Pattern Recognition*. 3691–3700.
- [38] Stephen Milborrow and Fred Nicolls. 2008. Locating Facial Features with an Extended Active Shape Model. In *European Conference on Computer Vision*, David A. Forsyth, Philip H. S. Torr, and Andrew Zisserman (Eds.), Vol. 5305. 504–513.
- [39] Alejandro Newell, Kaiyu Yang, and Jia Deng. 2016. Stacked Hourglass Networks for Human Pose Estimation. In *European Conference on Computer Vision*, Vol. 9912. 483–499.
- [40] Phuong Anh Nguyen, Qing Li, Zhi-Qi Cheng, Yi-Jie Lu, Hao Zhang, Xiao Wu, and Chong-Wah Ngo. 2017. Vireo@ TRECVid 2017: Video-to-text, ad-hoc video search and video hyperlinking. (2017).
- [41] Aiden Nibali, Zhen He, Stuart Morgan, and Luke A. Prendergast. 2018. Numerical Coordinate Regression with Convolutional Neural Networks. *CoRR abs/1801.07372* (2018).
- [42] Shengju Qian, Keqiang Sun, Wayne Wu, Chen Qian, and Jiaya Jia. 2019. Aggregation via Separation: Boosting Facial Landmark Detector With Semi-Supervised Style Translation. In *IEEE International Conference on Computer Vision*. 10152–10162.
- [43] Olaf Ronneberger, Philipp Fischer, and Thomas Brox. 2015. U-Net: Convolutional Networks for Biomedical Image Segmentation. In *Medical Image Computing and Computer-Assisted Intervention*. Springer, 234–241.
- [44] Olga Russakovsky, Jia Deng, Hao Su, Jonathan Krause, Sanjeev Satheesh, Sean Ma, Zhiheng Huang, Andrej Karpathy, Aditya Khosla, Michael Bernstein, Alexander C. Berg, and Li Fei-Fei. 2015. ImageNet Large Scale Visual Recognition Challenge. *International Journal of Computer Vision* 115, 3 (2015), 211–252.
- [45] Christos Sagonas, Epameinondas Antonakos, Georgios Tzimiropoulos, Stefanos Zafeiriou, and Maja Pantic. 2016. 300 Faces In-The-Wild Challenge: database and results. *Image and Vision Computing* 47 (2016), 3–18.

- [46] Guang-Lu Sun, Zhi-Qi Cheng, Xiao Wu, and Qiang Peng. 2018. Personalized clothing recommendation combining user social circle and fashion style consistency. *Multimedia Tools and Applications* 77 (2018), 17731–17754.
- [47] Ke Sun, Bin Xiao, Dong Liu, and Jingdong Wang. 2019. Deep High-Resolution Representation Learning for Human Pose Estimation. In *IEEE Conference on Computer Vision and Pattern Recognition*. 5693–5703.
- [48] Zhiqiang Tang, Xi Peng, Shijie Geng, Lingfei Wu, Shaoting Zhang, and Dimitris N. Metaxas. 2018. Quantized Densely Connected U-Nets for Efficient Landmark Localization. In *European Conference on Computer Vision*. 348–364.
- [49] Shuyuan Tu, Qi Dai, Zuxuan Wu, Zhi-Qi Cheng, Han Hu, and Yu-Gang Jiang. 2023. Implicit temporal modeling with learnable alignment for video recognition. *arXiv preprint arXiv:2304.10465* (2023).
- [50] Jun Wan, Jun Liu, Jie Zhou, Zhihui Lai, Linlin Shen, Hang Sun, Ping Xiong, and Wenwen Min. 2023. Precise Facial Landmark Detection by Reference Heatmap Transformer. *IEEE Transactions on Image Processing* 32 (2023), 1966–1977.
- [51] Xinyao Wang, Liefeng Bo, and Fuxin Li. 2019. Adaptive Wing Loss for Robust Face Alignment via Heatmap Regression. In *IEEE International Conference on Computer Vision*. 6970–6980.
- [52] Wayne Wu, Chen Qian, Shuo Yang, Quan Wang, Yici Cai, and Qiang Zhou. 2018. Look at Boundary: A Boundary-Aware Face Alignment Algorithm. In *IEEE Conference on Computer Vision and Pattern Recognition*. 2129–2138.
- [53] Jiahao Xia, Weiwei Qu, Wenjian Huang, Jianguo Zhang, Xi Wang, and Min Xu. 2022. Sparse local patch transformer for robust face alignment and landmarks inherent relation learning. In *IEEE/CVF Conference on Computer Vision and Pattern Recognition*. 4052–4061.
- [54] Feng Zhang, Xiatian Zhu, Hanbin Dai, Mao Ye, and Ce Zhu. 2020. Distribution-Aware Coordinate Representation for Human Pose Estimation. In *IEEE Conference on Computer Vision and Pattern Recognition*. 7091–7100.
- [55] Yuxuan Zhou, Zhi-Qi Cheng, Jun-Yan He, Bin Luo, Yifeng Geng, Xuansong Xie, and Margret Keuper. 2023. Overcoming Topology Agnosticism: Enhancing Skeleton-Based Action Recognition through Redefined Skeletal Topology Awareness. *arXiv preprint arXiv:2305.11468* (2023).
- [56] Yuxuan Zhou, Chao Li, Zhi-Qi Cheng, Yifeng Geng, Xuansong Xie, and Margret Keuper. 2022. Hypergraph transformer for skeleton-based action recognition. *arXiv preprint arXiv:2211.09590* (2022).
- [57] Zhenglin Zhou, Huaxia Li, Hong Liu, Nanyang Wang, Gang Yu, and Rongrong Ji. 2023. STAR Loss: Reducing Semantic Ambiguity in Facial Landmark Detection. In *IEEE/CVF Conference on Computer Vision and Pattern Recognition*. 15475–15484.
- [58] Meilu Zhu, Daming Shi, Mingjie Zheng, and Muhammad Sadiq. 2019. Robust Facial Landmark Detection via Occlusion-Adaptive Deep Networks. In *IEEE Conference on Computer Vision and Pattern Recognition*. 3486–3496.
- [59] Shizhan Zhu, Cheng Li, Chen Change Loy, and Xiaoou Tang. 2015. Face alignment by coarse-to-fine shape searching. In *IEEE Conference on Computer Vision and Pattern Recognition*. 4998–5006.
- [60] Shizhan Zhu, Cheng Li, Chen Change Loy, and Xiaoou Tang. 2015. Face alignment by coarse-to-fine shape searching. In *IEEE Conference on Computer Vision and Pattern Recognition*. 4998–5006.
- [61] Xu Zou, Sheng Zhong, Luxin Yan, Xiangyun Zhao, Jiahuan Zhou, and Ying Wu. 2019. Learning Robust Facial Landmark Detection via Hierarchical Structured Ensemble. In *IEEE International Conference on Computer Vision*. 141–150.